Article

Influence of Spring Precipitation over Maritime Continent and Western North Pacific on the Evolution and Prediction of El Niño–Southern Oscillation

Yifan Ma [1], Fei Huang [1,2] and Ruihuang Xie [1,2,*]

1 Department of Marine Meteorology, College of Oceanic and Atmospheric Sciences, Ocean University of China, Qingdao 266100, China; mayifan@stu.ouc.edu.cn (Y.M.); huangf@ouc.edu.cn (F.H.)
2 Frontier Science Center for Deep Ocean Multispheres and Earth System (FDOMES) and Physical Oceanography Laboratory, Ocean University of China, Qingdao 266100, China
* Correspondence: xieruihuang@ouc.edu.cn

Abstract: Previous studies suggested that spring precipitation over the tropical western Pacific Ocean can influence the development of El Niño–Southern Oscillation (ENSO). To identify crucial precipitation patterns for post-spring ENSO evolution, a singular value decomposition (SVD) method was applied to spring precipitation and sea surface temperature (SST) anomalies, and three precipitation and ENSO types were obtained with each highlighting precipitation over the Maritime Continent (MC) or western north Pacific (WNP). High MC spring precipitation corresponds to the slow decay of a multi-year La Niña event. Low MC spring precipitation is associated with a rapid El Niño-to-La Niña transition. High WNP spring precipitation is related to positive north Pacific meridional mode and induces the El Niño initiation. Among the three ENSO types, ocean current and heat content behave differently. Based on these spring precipitation and oceanic factors, a statistical model was established aimed at predicting winter ENSO state. Compared to a full dynamical model, this model exhibits higher prediction skills in the winter ENSO phase and amplitude for the period of 1980–2022. The explained total variance of the winter Niño-3.4 index increases from 43% to 75%, while the root-mean-squared error decreases from 0.82 °C to 0.53 °C. The practical utility and limitations of this model are also discussed.

Keywords: spring precipitation; ENSO evolution; Maritime Continent; western north Pacific; sea current; warm water volume; ENSO prediction

1. Introduction

The El Niño–Southern Oscillation (ENSO) is one of the most energetic coupled ocean–atmosphere phenomena on Earth, profoundly shaping global weather, climate and ocean conditions [1]. ENSO manifests as a cyclical alternation between anomalous warm (El Niño) and cold (La Niña) conditions in the tropical Pacific, recurring approximately every two to seven years [1–3]. Given its significant socioeconomic impacts, extensive research efforts have been dedicated to improving our understanding of its mechanisms and long-lead forecasts.

Situated at the transition zone between the Indo–Pacific warm pool and Asia–Australia, the Maritime Continent (MC) displays a complex topography characterized by numerous islands and shallow but warm seas (Figure 1). Evaporation from the warm seas supplies water vapor and heat flux to the atmosphere, which generates ascending moist air and intense precipitation in the ascending branch of Walker circulation (Figure 1). The precipitation over the MC can yield a substantial influence on the global climate [4]. The precipitation over the MC is primarily modulated by ENSO on interannual timescales [5–8]. During winter (December–January–February, DJF) and the following spring (March–April–May, MAM) of El Niño, positive sea surface temperature anomalies (SSTAs) in the central and

eastern tropical Pacific shift Walker circulation eastwards. It leads to anomalous descending motion and suppressed precipitation over MC and the western north Pacific (WNP) [9,10]. During La Niña, the Walker circulation strengthens locally, which results in increased precipitation over the MC and WNP [11].
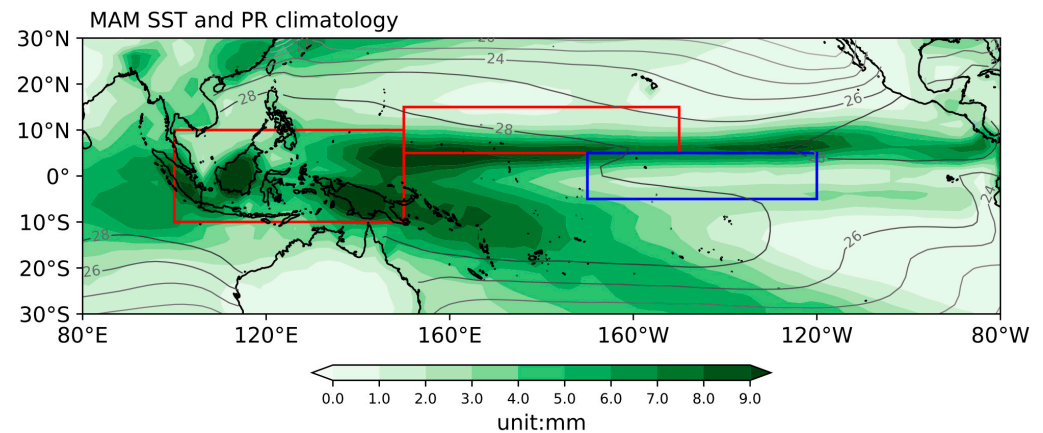

Figure 1. The climatological precipitation (shading, unit: mm) and sea surface temperature (gray contour, unit: °C) in the tropical Pacific during March–April–May (MAM) for the period of 1990–2022. Red boxes denote the regions of MC (10° S–10° N, 100–150° E) and WNP (5–15° N, 150° E–160° W), and the blue box indicates Niño-3.4 region (5° S–5° N, 170° W–120° W).

On the other hand, spring precipitation over the MC can also influence the evolution of ENSO, particularly during the decay phase of El Niño. When spring MC precipitation is suppressed by anomalously descending motion driven by El Niño through the pair of off-equatorial anticyclones [9,10], the low-level easterly anomalies over the equatorial western Pacific can excite upwelling oceanic Kelvin waves to propagate eastwards to weaken El Niño by a shoaling thermocline and enhancing oceanic upwelling in the eastern Pacific [12–14]. On the contrary, when spring MC precipitation is increased in spring by La Niña, the low-level westerly anomalies over the equatorial western Pacific can excite downwelling oceanic Kelvin waves to cause a warming tendency in the equatorial eastern Pacific through a deepening thermocline and suppress oceanic upwelling.

On interannual timescales, the WNP spring precipitation can be controlled by two air–sea interactive modes: the North Pacific meridional mode (NPMM) [15–18] and the existing ENSO [9,19–22]. Triggered by extra-tropical atmospheric variability in winter, NPMM SSTA propagates southwestwards via the wind–evaporation–SST (WES) feedback and reaches the equatorial western Pacific in spring [15,23–26]. Those SSTAs induce precipitation anomalies by generating off-equatorial atmospheric Rossby waves over the WNP [27], which further projects low-level wind anomalies over the equatorial western Pacific. Subsequently, ENSO occurs as a result of the eastward propagating oceanic Kelvin waves. However, many studies indicated that NPMM shows spatial diversity, and only those with SSTA in the western equatorial Pacific in spring (about 50% of total NPMM events) are capable of triggering ENSO in the following winter [24,28,29]. Therefore, spring WNP precipitation anomalies, as a result of the NPMM-related SSTA in the western Pacific, may be a more effective predictor for ENSO than NPMM itself. Moreover, spring WNP precipitation is also influenced by the existing ENSO event. An anomalous anticyclone (cyclone) persists from the preceding winter to spring when an El Niño (a La Niña) event occurs [9,19]. Therefore, the anomalous easterlies (westerlies) at the south part of the anomalous anticyclone (cyclone) can generate equatorial upwelling (downwelling) oceanic Kelvin waves to weaken the existing El Niño (La Niña) [30,31]. During El Niño decaying spring, such an anomalous WNP anticyclone and suppressed precipitation are also accompanied by the southward shift of westerly and positive precipitation anomalies over the equatorial central Pacific [32–35], which result from the nonlinear interaction between ENSO and the

annual cycle [20–22]. Due to the seasonal southward migration of the solar radiation from winter to spring, El Niño SSTA south of the equator is located in a higher background SST, leading to higher convection sensitivity and greater precipitation anomalies than those at the north [36]. Such a southward shift of westerly anomalies in spring induces a weakening of westerly anomalies along the equator, which can further accelerate the decaying of El Niño [22]. But during La Niña decaying spring, the anomalous WNP cyclone and the southward shift of easterly anomalies over the central Pacific are much weaker than the opposite patterns during El Niño [19,35,37], the decaying trend of La Niña is therefore weaker. These differences in wind may be responsible for the persistence of multi-year La Niña events.

During the evolution of ENSO, the oceanic conditions in spring also contribute, such as the warm water volume (WWV: the volume of water above the 20 °C isotherm in the tropical Pacific) [38–41] and sea surface zonal currents [42–44]. The effects of WWV and sea surface zonal currents, corresponding to thermocline feedback and zonal advective feedback, have been regarded as the two major contributors to ENSO evolution [44,45]. Observations indicate that the variation of WWV leads ENSO by 2–3 seasons [40,46], making spring WWV a good indicator for winter ENSO state [44,47]. Furthermore, the variations in WWV and sea surface zonal current are interrelated [48], as they both depend primarily on changes in the thermocline, which is correlated with zonal wind stress over the equatorial central and western Pacific [38,39,48].

It has been clear that the variation in spring precipitation over the MC and WNP can influence ENSO evolution, but previous studies either treated MC and WNP as an entire region or focused on either one, as in the aforementioned literature. In this study, we re-examine the patterns of spring precipitation over MC and WNP and propose that the spring precipitation patterns over these two regions have an independent influence on ENSO evolution.

2. Materials and Methods

Atmospheric and oceanic variables, such as SST, wind, precipitation, sea current and ocean potential temperature, are used to explore the air–sea coupling processes during the evolution of ENSO. The monthly precipitation data used in this study are from the Global Precipitation Climatology Project (GPCP) [49]. Low-level wind data are from the National Centers for Environmental Prediction (NCEP)–National Center for Atmospheric Research (NCAR) Reanalysis 2 dataset [50]. These data have a $2.5° \times 2.5°$ latitude–longitude grid. SST in the same period is from the National Oceanic and Atmospheric Administration (NOAA) Extended Reconstructed Sea Surface Temperature version 5 (ERSSTv5) dataset [51], which is in a $2° \times 2°$ longitude–latitude grid. WWV and sea surface currents are calculated from the NCEP Global Ocean Data Assimilation System (GODAS) [52]. This study covers the period of 1980–2022 when various satellite and in situ datasets are assimilated for high data quality. All monthly data are linearly de-trended, and a 3-month running mean is applied to remove the intraseasonal variation. Monthly anomalies are obtained by removing the corresponding climatological monthly mean calculated in the base period of 1991–2020.

The Niño-3.4 index, defined as the average SSTA in the equatorial central-to-eastern Pacific (5° S–5° N, 170° W–120° W), is used to identify an ENSO event. According to the NOAA Climate Prediction Center, an ENSO event is identified when the 3-month running-mean Niño-3.4 index exceeds a threshold of ± 0.5 °C for 5 consecutive overlapping months. Due to phase locking of ENSO with its peak in boreal winter [53], DJF Niño-3.4 index is used to measure the amplitude of ENSO.

Singular Value Decomposition (SVD) is employed to investigate the coupling processes between spring precipitation over the tropical western Pacific and SST in the entire tropical Pacific. SVD has been used widely in the atmospheric and oceanic sciences [54,55], with the purpose of extracting the co-varying patterns in two different fields with different spatial domains. It decomposes the covariance matrix of two fields into singular values and two

sets of paired-orthogonal vectors (also called modes), one for each field. The modes are ordered depending on the amount of squared covariance explained. It is worth noting that SVD suffers from a strong orthogonality constraint, so it may produce results inconsistent with real physical processes. Composite analysis is also applied based on the first two SVD modes to confirm results containing meaningful connections between precipitation and SST fields.

3. Results

3.1. Spring Precipitation Patterns over MC and WNP

Figure 2 shows the first two SVD modes of the spring (MAM) precipitation patterns over the western tropical Pacific (20° S–20° N, 80° E–120° W) and SSTA in the entire tropical Pacific (30° S–30° N, 120° E–80° W), which explains about 44% of the total covariance. The pattern of precipitation in the first mode shows a zonal dipole precipitation pattern with negative anomalies over MC (10° S–10° N, 100–150° E) and positive anomalies over the western Pacific (5° S–5° N, 160° E–160° W) (Figure 2a), while those of SSTA display an El Niño-like pattern with positive (negative) SSTA in the tropical central-to-eastern (western) Pacific (Figure 2b). The corresponding timeseries of precipitation (hereafter PR_{PC1}) and SST anomalies are highly correlated ($r = 0.93$), and both show high values in the springs following ENSO events (Figure 2c). This suggests that this mode corresponds to an air–sea interactive pattern when ENSO decays.
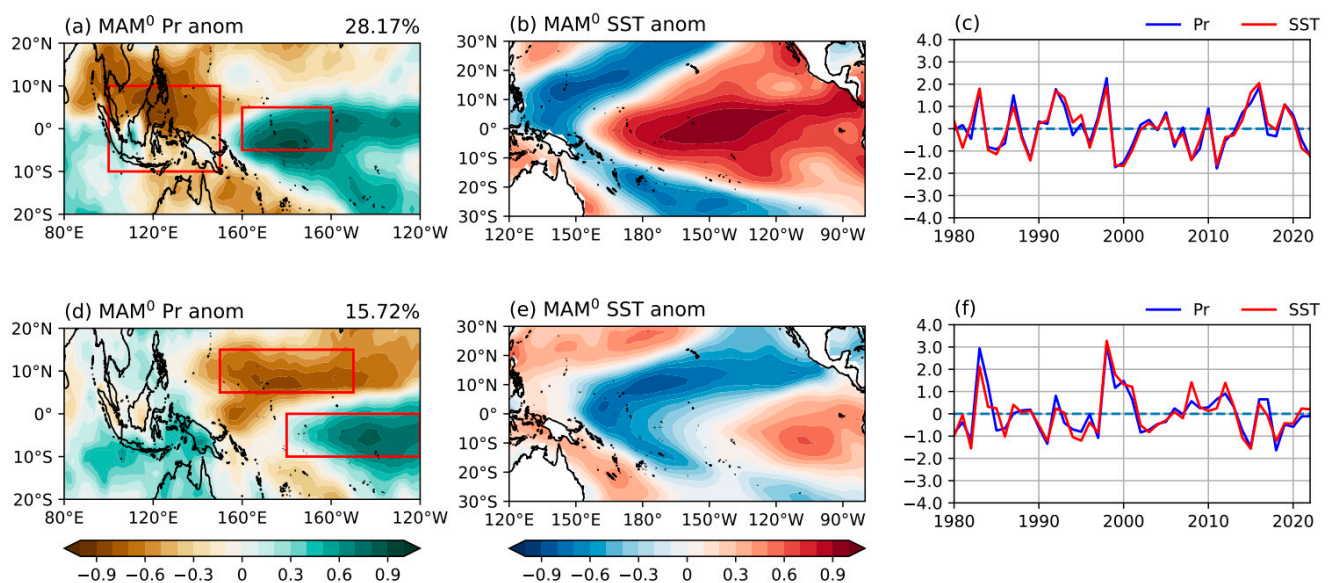

Figure 2. Spatial patterns of the first two SVD modes of spring precipitation (**a**,**d**) and SST (**b**,**e**) anomalies, and their expansion coefficients (**c**,**f**). The upper and lower panel corresponds to the first and second SVD mode, respectively. The red boxes in (**a**) denote the regions of 10° S–10° N, 100–150° E and 5° S–5° N, 160° E–160° W that represent the poles of precipitation anomalies, and the red boxes in (**d**) are for the precipitation poles in 5–15° N, 150° E–160° W and 0–10° S, 180–120° W. Spatial patterns are the heterogeneous correlation maps that are dimensionless.

In contrast, the second mode of spring precipitation shows a tilted meridional pattern over the tropical Pacific, characterized by negative precipitation anomalies over WNP (5–15° N, 150° E–150° W) and positive anomalies over the tropical central Pacific south of the equator (0–10° S, 180–120° W) (Figure 2d). The corresponding SSTA exhibits a pattern similar to negative NPMM, with negative SSTA extending from the western coast of North America to the equatorial western Pacific and weak positive SSTA in the tropical eastern Pacific (Figure 2e). The spring NPMM has been considered a linkage between extra-tropical atmospheric variability and ENSO through exciting equatorial Kelvin waves from the equatorial western Pacific to change SST in the east [26]. The timeseries of precipitation

(hereafter PR$_{PC2}$) and SST anomalies are also highly correlated (r = 0.87) (Figure 2f), and they show high positive values in the decaying springs of strong El Niño events, such as in 1983 and 1998.

However, SVD also produces unreasonable signals. Based on the criteria of the PR$_{PC1}$ and PR$_{PC2}$ values exceeding ± 0.8 standard deviations, the identified ENSO events show a large overlap across the four precipitation groups (see Table 1). It seems that SVD projects real precipitation and SST signals into several components in major ENSO events. For instance, precipitation decreases over the entire western tropical Pacific in the decaying springs of strong El Niño events in 1983 and 1998 due to the anomalously strong anticyclone over the MC and WNP [22]. Therefore, the springs of 1983, 1998, and 2016 fall into both the low MC precipitation group and low WNP precipitation group. The recent extreme El Niño in 2015/16 is somehow different from the 1982/83 and 1997/98 extreme El Niño events in its spatial pattern and amplitude [56–59], but the anomalous precipitation over the western tropical Pacific still shows similarity [60]. La Niña events locate in a more westward location than El Niño events in the mature winter and decaying spring [61,62] (also see Figure 3b); precipitation decreases over WNP and equatorial central Pacific but increases over MC (Figure 3a), which is a typical response to during La Niña [19]. Thus, the La Niña springs in 1984, 1999, and 2000 are identified as either the high MC precipitation group or the low WNP precipitation group. Therefore, the identified El Niño events in the low WNP precipitation group will be reassigned to the low MC precipitation group, while the La Niña events are moved into the high MC precipitation group. The spring of 1993 experienced a short return of weak El Niño in the tropical central Pacific that gradually relaxed to a neutral condition in winter [63], while the spring of 2015 followed the stalled El Niño in 2014 that projected a weak positive SSTA in the tropical central-to-eastern Pacific in early 2015 [64]. Due to the distinct El Niño evolution, the springs of 1993 and 2015 will be excluded from the low MC precipitation group in this analysis.

Table 1. Individual El Niño–Southern Oscillation (ENSO) events in the classified groups.

Precipitation (PR) Groups	Criteria	Individual ENSO Events in Spring
high MC PR group	PR$_{PC1}$ < −0.8	1984 *, 1985, 1989, 1999 *, 2000 *, 2001, 2006, 2008, 2009, 2011
low MC PR group	PR$_{PC1}$ > 0.8	1983 *, 1987, 1992, 1993, 1998 *, 2010, 2015 *, 2016, 2019
high WNP PR group	PR$_{PC2}$ < −0.8	1980, 1982, 1991, 1997, 2002, 2015 *, 2018
low WNP PR group	PR$_{PC2}$ > 0.8	1983 *, 1984 *, 1998 *, 1999 *, 2000 *

Asterisk (*) indicates event that is overlapped across different groups.

Therefore, there are, in fact, three spring precipitation groups related to ENSO without overlap of individual events (see Table 2). ENSO events in the high spring MC precipitation group are those following the mature winters of La Niña events. The precipitation pattern is featured as increased (decreased) precipitation over the MC (equatorial central-to-eastern Pacific) (Figure 3a), and the related SSTA pattern shows a broad negative SSTA over the tropical central-to-eastern Pacific, with maximal values around the dateline (Figure 3b). Conversely, ENSO events in the low spring MC precipitation group are the decaying El Niño events, characterized by less (more) precipitation over the MC and WNP (equatorial central-to-eastern Pacific) (Figure 3c) and positive SSTA to the east of the dateline (Figure 3d). For the high spring WNP precipitation group, the related precipitation anomalies manifest as a tilted meridional pattern, with increased precipitation over WNP and decreased rainfall over MC and central Pacific to the south of the equator (Figure 3e). The associated SSTA pattern resembles positive NPMM, featured as positive SSTA extending from the tropical northeastern Pacific to the equatorial western Pacific and slightly negative SSTA in the tropical eastern Pacific (Figure 3f).
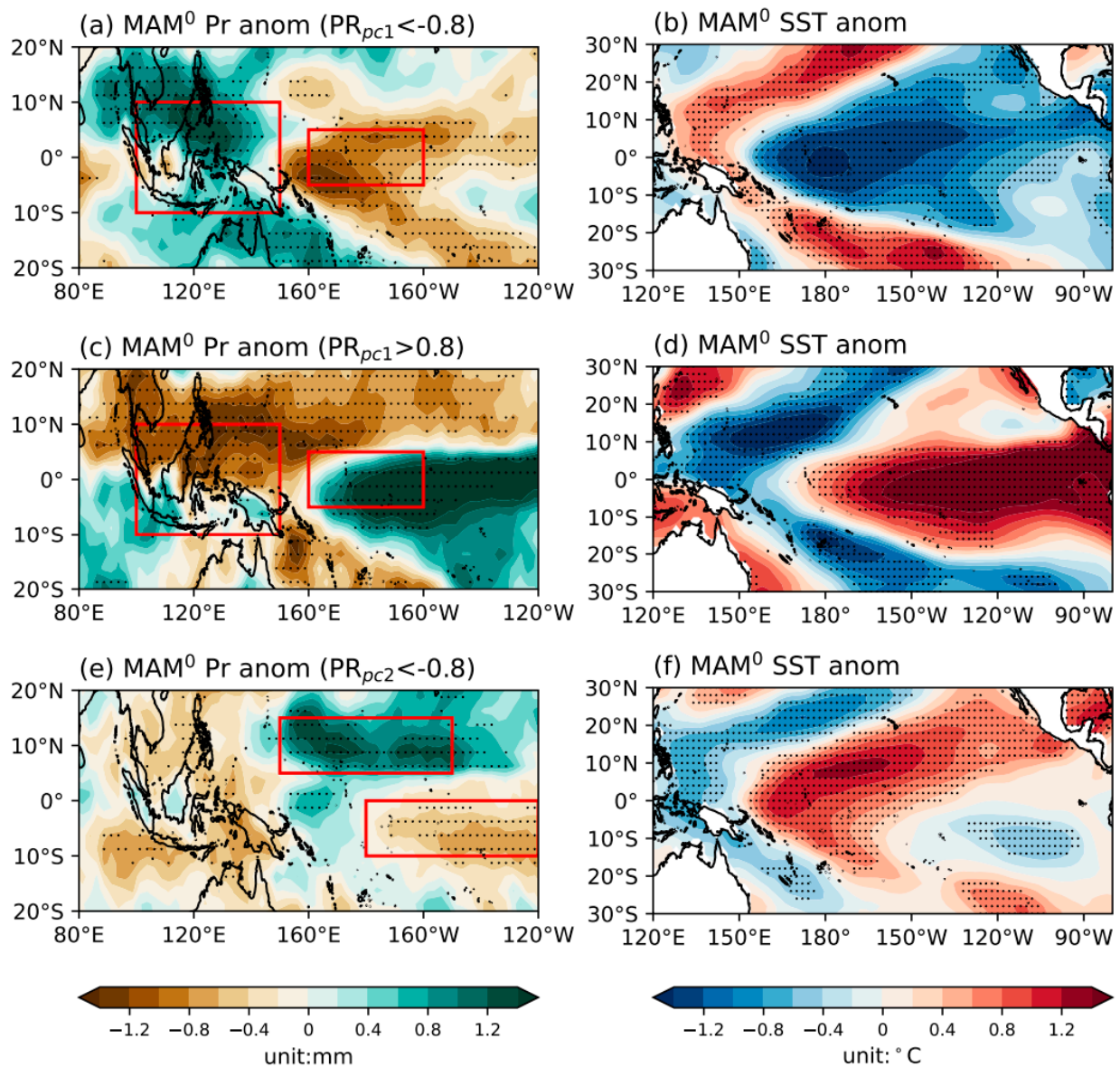
Figure 3. Composites of spring precipitation ((**a**,**c**,**e**), unit: mm) and sea surface temperature (SST) ((**b**,**d**,**f**), unit: °C) anomalies in the tropical Pacific for the classified ENSO groups. The red boxes in (**a**,**c**) denote the regions of 10° S–10° N, 100–150° E and 5° S–5° N, 160° E–160° W that represent the poles of precipitation anomalies, and the red boxes in (**e**) are for the precipitation poles in 5–15° N, 150° E–160° W and 0–10° S, 180–120° W. The black dots represent the values exceeding the 95% confidence levels estimated from a two-tailed Student's *t*-test.

Table 2. Corrected spring precipitation groups and the associated El Niño–Southern Oscillation (ENSO) events.

Precipitation (PR) Groups	Criteria	Individual ENSO Event in Spring
high MC PR group	$PR_{PC1} < -0.8$	1984, 1985, 1989, 1999, 2000, 2001, 2006, 2008, 2009, 2011
low MC PR group	$PR_{PC1} > 0.8$	1983, 1987, 1992, 1998, 2010, 2016, 2019
high WNP PR group	$PR_{PC2} < -0.8$	1980, 1982, 1991, 1997, 2002, 2015, 2018

3.2. Linkages between Spring MC Precipitation and ENSO Evolution in Subsequent Seasons

In order to obtain the complete evolution of precipitation over the tropical western Pacific and the associated ENSO conditions, seasonal composites of these two fields and

oceanic factors, including WWV and sea surface currents, are applied with several seasons before and after MAM^0. The identified high MC precipitation group contains springs of decaying La Niña. As shown in Figure 4, spring (MAM^0) precipitation anomalies exhibit a zonal dipole pattern, with positive precipitation anomalies over MC and negative anomalies over the equatorial western Pacific (Figure 4e). This precipitation pattern evolves from a tilted meridional pattern in the preceding spring (MAM^{-1}) that resembles the second SVD mode (Figure 4a), whereas the associated SSTA manifests as a negative NPMM (Figure 4i). In the subsequent seasons from JJA^{-1} to $D^{-1}JF^0$, negative NPMM develops into a La Niña event (Figure 4i–l), which is amplified by negative WWV that supplies anomalously cool subsurface water upwards, and the westward sea surface currents along the equator that transport cool water westwards from the cold tongue (Figure 4q–t). During the development of La Niña, the tilted meridional precipitation pattern evolves rapidly into a zonal pattern between the MC and equatorial western Pacific (Figure 4a–d) due to the enhancement of the low-level moist convergence (divergence) over the MC (equatorial western Pacific) facilitated by low-level easterly anomalies over the central-to-western Pacific (Figure 4i–l). In turn, the zonal precipitation dipole pattern maintains and enhances the westward sea current anomalies.

In the mature phase of La Niña ($D^{-1}JF^0$), WWV in the western Pacific turns positive (Figure 4t), attributed to the accumulation of oceanic heat content transported by the westward sea current anomalies in the preceding seasons (Figure 4q–t). Meanwhile, local equatorial sea current anomalies reverse eastwards, partly due to the zonal pressure gradient of sea surface height along the equator [42,43] and partly due to the reflected downwelling equatorial oceanic Kelvin waves from the downwelling off-equatorial Rossby waves at the western boundary. Such eastward sea current anomalies tend to weaken La Niña (Figure 4m,n) by transporting warm water and heat content eastwards from the warm pool (Figure 4u,v). It is observed that the reversal of sea currents leads to the change of WWV, consistent with the analysis of Ren and Jin [47], who suggested a dominant role in the reversal of sea current anomalies in the ENSO phase transition. However, it is noteworthy that a negative NPMM-like SSTA pattern is evident during the decaying spring of La Niña (see Figure 4m). The negative NPMM is regarded as an important contributor to negative SSTA in the equatorial central-to-western Pacific [26,65,66] by generating and maintaining local easterly anomalies. Despite the warming tendencies by sea current reversal, negative SSTA in the equatorial central-to-western Pacific and zonal precipitation dipole pattern persists throughout the entire year (Figure 4d–h), the low-level easterly anomalies consequently persist over the equatorial central Pacific (Figure 4m–p), which tends to generate westward sea current anomalies to weaken the equatorial eastward current anomalies in the central Pacific (Figure 4u–w). Consequently, La Niña decays slowly in the following seasons.

For the low MC precipitation group, the springs are those when El Niño decays (Figure 5m). The precipitation anomalies are characterized by decreased (increased) precipitation over the MC (tropical western Pacific) (Figure 5e). In the preceding spring (MAM^{-1}), the precipitation anomalies manifest as a tilted meridional dipole pattern with more (less) precipitation over the WNP (tropical central Pacific) (Figure 5a), attributed to the positive NPMM (Figure 5i). Meanwhile, the equatorial Pacific is in a recharged state, featured as a basin-wide positive WWV (Figure 5q), which is regarded as a favorable condition for El Niño onset [38,40]. Furthermore, the anomalous eastward sea currents can advect warm water from the warm pool to the cold tongue (Figure 5q). Therefore, El Niño enhances in the subsequent seasons (Figure 5j,k). Due to increases in SSTA in the equatorial central-to-eastern Pacific, precipitation intensifies locally, and the tilted meridional dipole pattern changes to a zonal dipole pattern (Figure 5b–d).
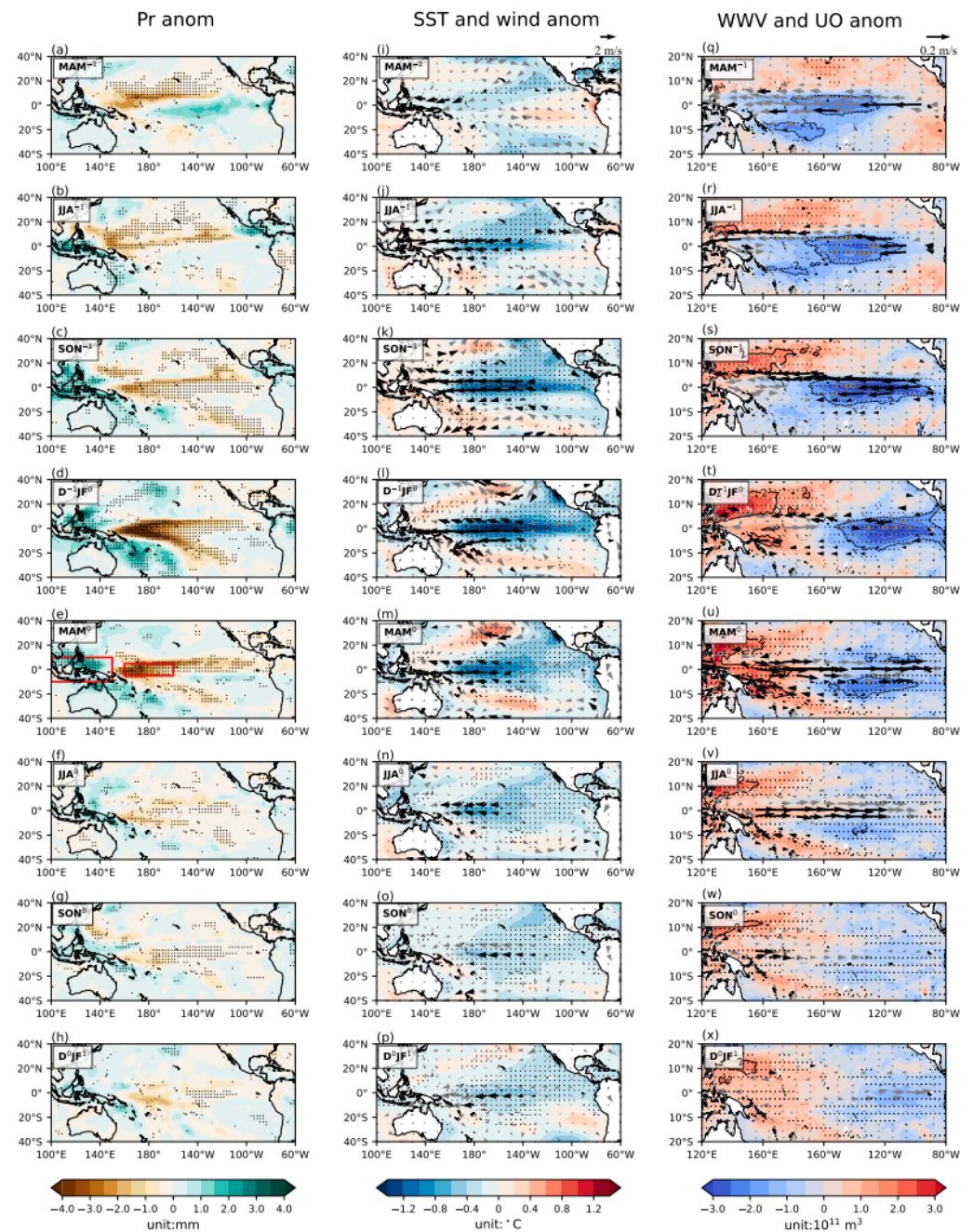
Figure 4. Composite evolution of anomalous precipitation (Pr, shading in the **left** panel, mm), sea surface temperature (SST, shading in the **middle** panel, °C), wind at 850 hPa (vectors in the **middle** panel, m/s), warm water volume (WWV, shading in the **right** panel, 10^{11} m^3), and zonal sea current averaged in the upper 50 m layers (UO, vectors in the **right** panel, m/s) for the high Maritime Continent (MC) precipitation group. The panel with red boxes denotes the spring of each identified event. The black dots in all panels and black vectors in the **middle** and **right** panels represent the values exceeding the 95% confidence levels estimated from a two-tailed Student's *t*-test, and gray vectors are for those under the 95% confidence levels.

In the mature winter ($D^{-1}JF^0$) and decaying spring (MAM^0) of El Niño, the maximal positive precipitation and westerly anomalies shift south of the equator (3~5° S) over the central Pacific (Figure 5d,e,l,m), due to the southward shift of the high SST driven by the seasonal southward migration of solar radiation [22,67]. Such a southward shift of westerly anomalies collapses the balance between the zonal gradient of sea surface height

and wind stress along the equator, leading to a net westward pressure gradient and sea surface current anomalies [43] (see also in Figure 5t,u). Furthermore, the southward shift of westerly anomalies also enhances poleward Sverdrup transports [68], which could intensify the discharge of equatorial WWV and heat content in the equatorial central Pacific. The joint cooling effects of anomalous westward sea currents and negative WWV result in the decaying of El Niño in the equatorial central Pacific in spring (MAM^0; Figure 5m). Meanwhile, the negative precipitation anomalies over MC induce anomalous easterlies over the far western Pacific (Figure 5m). These easterlies generate upwelling oceanic Kelvin waves to propagate eastwards to shoal the thermocline and reduce the WWV in the eastern Pacific, leading to the decay of positive SSTA in the far eastern Pacific in the following summer (Figure 5n).
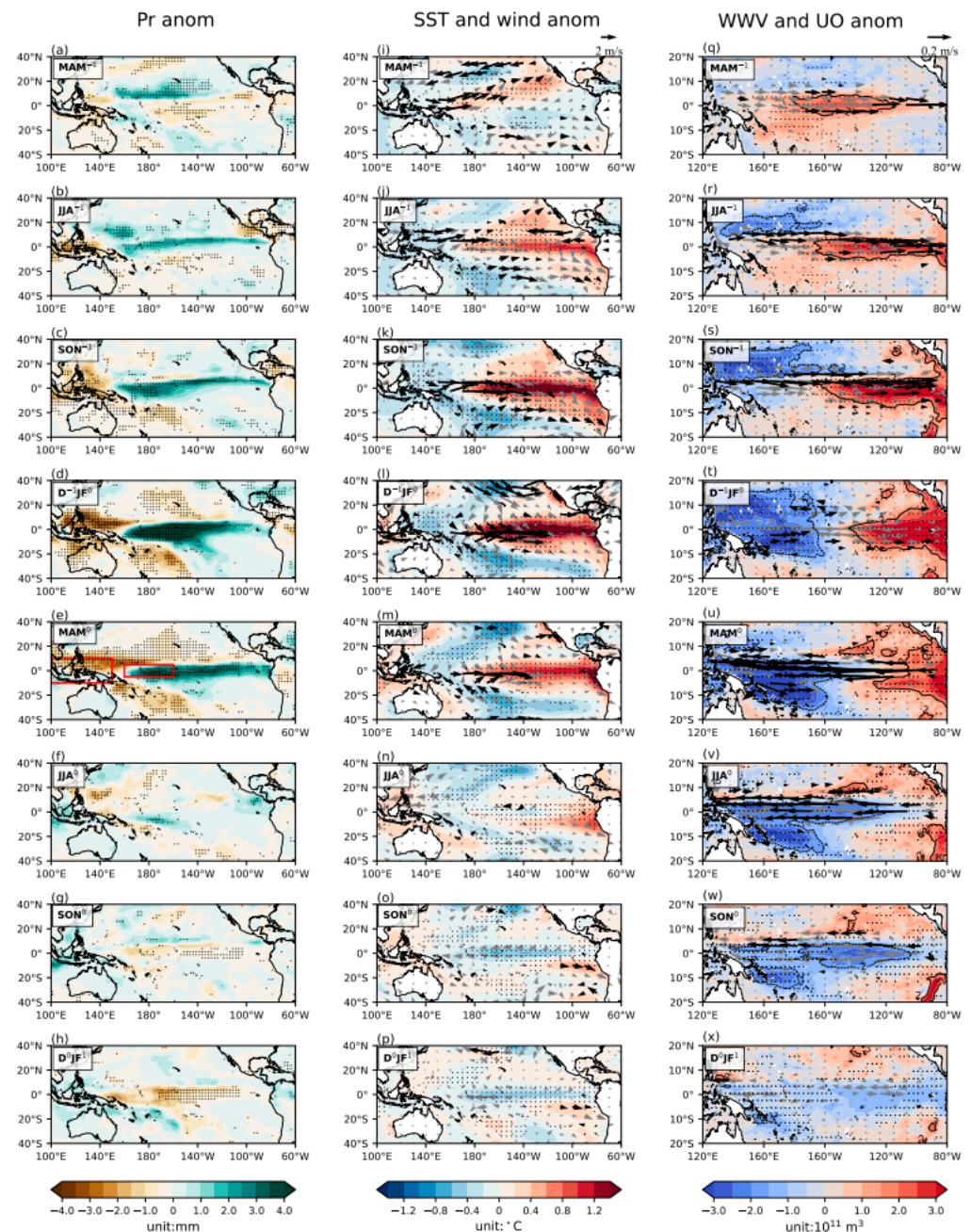

Figure 5. Same as Figure 4, but for the composite in the low Maritime Continent (MC) precipitation group.

Due to the persistence of the westward sea current and negative WWV anomalies in fall (SON; Figure 5w), La Niña develops. As a result, precipitation is reduced over the cooler equatorial central-to-western Pacific, which further induces anomalous easterlies (Figure 5g). Meanwhile, such easterly anomalies enhance the westward water vapor transport, resulting in increased precipitation over MC (Figure 5g). As La Nina matures in winter (D^0JF^1; Figure 5p), a zonal precipitation dipole pattern is established, with increased (decreased) precipitation over the MC (equatorial central-to-western Pacific) (Figure 5h), which is a typical precipitation pattern during La Nina winter (see Figure 4d).

3.3. Connections between Spring WNP Precipitation and ENSO Evolution

As displayed in Table 2, the individual events in the high WNP precipitation group are developing El Niño events in spring. A large portion of these events coincide with the events decaying in the next spring that are classified in the low MC precipitation group, such as the El Niño events initiating in 1982, 1991, 1997, 2015 and 2018. Therefore, as shown in Figure 6, the composite evolution of El Niño events in this group is similar to the low MC precipitation group present in Figure 5. El Niño develops from a positive NPMM in spring (Figure 6j), and this NPMM initiates in the preceding winter (Figure 6i) when an anomalous cyclone occurs over the north Pacific. The anomalous southwesterlies at the southeastern flank of the cyclone can reduce the wind speed of the mean northeasterlies in winter, which further reduces evaporation and warms the underlying SST [26]. Therefore, the positive NPMM enhances in the following spring, and the positive SSTA generates increased precipitation over the WNP (Figure 6b), which further triggers equatorial westerly anomalies over the western Pacific (Figure 6j). Equatorial downwelling Kelvin waves are subsequently excited to deepen the thermocline, enhance WWV and trigger eastward sea current anomalies in the tropical central-to-eastern Pacific (Figure 6r), creating a favorable condition for El Niño onset [39,40].

Additionally, these westerly anomalies also excite upwelling off-equatorial Rossby waves to propagate westwards to shallow the thermocline and decrease WWV in the western Pacific (Figure 6r–u). Due to these wave activities, the basin-wide positive WWV pattern in spring gradually transitions into a zonal dipole WWV pattern from summer to winter (Figure 6s–u). Therefore, the mean oceanic upwelling in the equatorial eastern Pacific advects the anomalously warmer water upwards to heat the sea surface, thus enhancing El Niño. During the development of El Niño, the precipitation anomalies gradually develop into a zonal dipole pattern (Figure 6c–e). After the mature winter (D^0JF^1), El Niño decays due to the anomalous westward sea currents in the equatorial eastern Pacific (Figure 6u) and the southward shift of westerly anomalies over the central Pacific (Figure 6m). The El Niño decaying pattern and mechanism are almost the same as those analyzed in the low MC precipitation group.

It is noteworthy again that there is no ENSO group with low WNP spring precipitation, as shown in Table 2. If ENSO is a linear oscillation, the low WNP spring precipitation group is expected to include La Niña events that transition to El Niño. However, the raw ENSO classification in Table 1 indicates that there is no such transition but contains a multi-year La Niña. It indicates the evolution asymmetry between El Niño and La Niña, primarily attributed to the fact that the heat content discharge process during El Niño is stronger and faster than the recharge counterpart during La Niña [69]. As displayed in Figure 5l,m, the westerly anomalies in the peak winter and decaying spring of El Niño suffer a sudden southward shift, leading to enhanced wind stress curl and northward Sverdrup transports of seawater mass and heat content. It accelerates the discharge process and induces a rapid phase transition. However, the anomalous easterlies related to La Niña are weaker, suggesting a slower recharge process. Furthermore, such La Niña easterly anomalies do not evidently shift southwards in the peak and decaying phases of La Niña (Figure 4l,m), leading to no acceleration of the recharge process. Therefore, the asymmetric discharge/recharge processes associated with the strength and meridional location of

anomalous wind are responsible for the disappearance of the ENSO group expected to exhibit La Niña transition to El Niño.
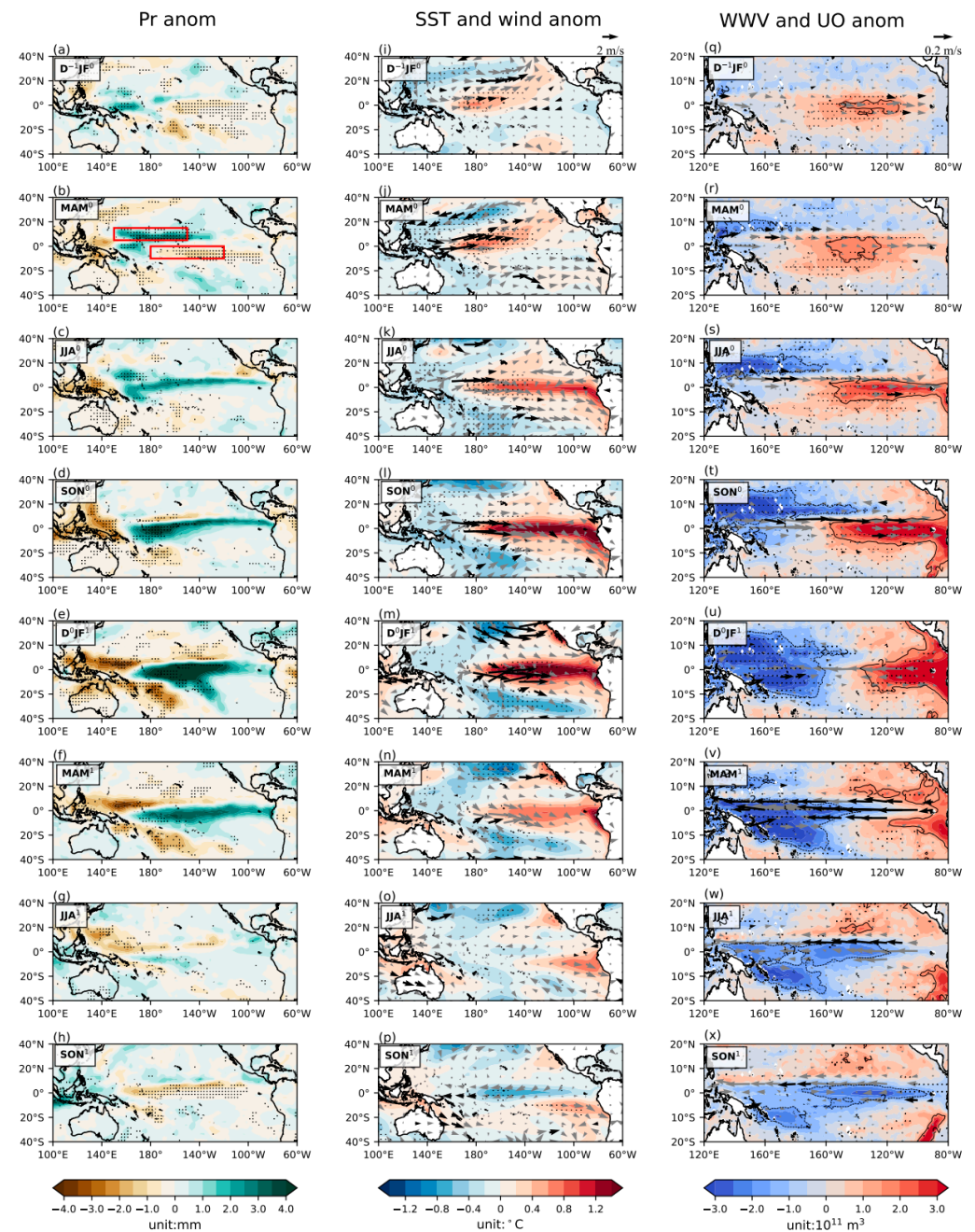

Figure 6. Same as Figure 4, but for the composite in the high western north Pacific (WNP) precipitation group.

3.4. Spring Precursors of ENSO Events

So far, three types of ENSO evolution have been identified based on the anomalous spring precipitation patterns over MC and WNP. They are spring precipitation patterns favoring the persistence of La Niña, decaying of El Niño and initiation of El Niño, respectively. These patterns highlight their roles in generating anomalous wind over the western-to-central equatorial Pacific, which could further excite oceanic waves and sea currents to change SSTA. Notably, there are robust connections between the spring precipitation, WWV, sea currents and the following winter (D^0JF^1) ENSO states (Figure 7). Spring precipitation over MC and WNP demonstrates a see-saw pattern, exhibiting a negative

(positive) connection between spring MC (WNP) precipitation and the subsequent winter ENSO state (Figure 7a).
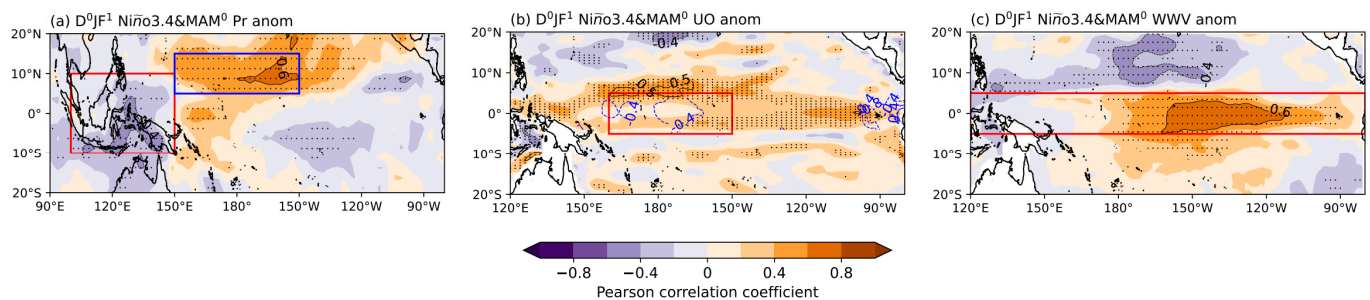

Figure 7. Correlation coefficients (shaded) between D^0JF^1 Niño-3.4 and MAM^0 (**a**) precipitation (Pr), (**b**) zonal current (UO), and (**c**) warm water volume (WWV) anomalies. Red and blue boxes in (**a**) represent the regions used to define the precipitation indices for the Maritime Continent (MC) and western north Pacific (WNP), respectively. Blue contour in (**b**) indicates the mean sea surface temperature (SST) gradient during MAM^0 (10^{-3} °C m^{-1}; only the values between 5° S and 5° N are displayed). Red box in (**c**) indicates the region for calculating WWV index. The black-dotted areas are for the values above the 95% confidence levels estimated from a two-tailed Student's *t*-test.

Furthermore, spring zonal sea currents display a basin-wide positive correlation with the subsequent winter ENSO state (Figure 7b), particularly pronounced in the equatorial Pacific. It reflects the role of eastward equatorial sea current anomalies in enhancing El Niño (Figure 6) and the role of westward currents in weakening El Niño (Figure 5) and intensifying La Niña (Figure 4). In spring, such sea current anomalies extend into the central Pacific, where the climatological SST gradient is the strongest (red box in Figure 7b). The anomalous eastward warm advection can induce a strong warming tendency in the equatorial central Pacific. Furthermore, spring WWV exhibits a nearly basin-scale positive correlation with the subsequent winter ENSO state, with the highest correlation observed east of the dateline (Figure 7c). This reaffirms the role of WWV in the recharge–discharge ENSO theory [38–40], wherein the recharged heat content in the equatorial Pacific during spring would lead to an El Niño in winter, and the discharged state leads to La Niña.

3.5. A Simple Statistical Model for Predicting ENSO

Many statistical and dynamical models in previous studies have displayed a relatively high skill in predicting ENSO [41,70,71]. However, our primary objective remains to enhance the accuracy of prediction in both the ENSO phase and amplitude. Our analyses have revealed that the spring MC and WNP precipitation patterns exert a notable influence on ENSO evolution. Additionally, we have presented evidence highlighting the relationship between spring WWV, zonal sea current and ENSO thus far. Building upon these insights, we subjected these findings to a rigorous test through a straightforward predictive exercise, aiming to quantify the relative contributions of those spring atmospheric and oceanic factors in long-lead ENSO prediction.

A simple multivariate statistical model is established in the following expression,

$$
\begin{aligned}
SSTA_{D0JF1}(x,t) = a(x) \times PR^{MC}_{MAM0}(t) + b(x) \times PR^{WNP}_{MAM0}(t) + c(x) \times WWV_{MAM0}(t) \\
+ d(x) \times UO_{MAM0}(t) + \varepsilon,
\end{aligned}
\tag{1}
$$

where *x* is the spatial coordinate, *t* is time and *a*, *b*, *c* and *d* denote the regression coefficients for the four precursors determined through least squares fitting. The precipitation factors (PR^{MC} and PR^{WNP}) are the averaged values over MC and WNP (boxes in Figure 7a), the sea current factor (UO) is the mean value in the equatorial central Pacific (red box in Figure 7b), and the WWV factor is the mean value averaged between 5° S and 5° N in the entire equatorial Pacific (red box in Figure 7c). It was suggested that the effective lead-time of

ENSO prediction is up to 20 months, depending on the analysis tools and length of the ENSO record [56,72–74]. Therefore, the adoption of a lead-time of two seasons in our prediction is expected to exhibit a high prediction skill.

Due to the evolution asymmetry between El Niño and La Niña after spring, as analyzed above, separate hindcasts were designed for El Niño and La Niña events with different coefficients in Equation (1). For instance, the coefficients for El Niño hindcast were obtained by multiple linear regression of the four spring factors onto the winter Niño-3.4 index that is greater than 0.5 °C. The coefficient values for El Niño and La Niña hindcasts are shown in Table 3.

Table 3. Coefficient values used for separate Niño-3.4 prediction in El Niño and La Niña hindcasts.

ENSO Phase	a ($°C \; mm^{-1}$)	b ($°C \; mm^{-1}$)	c ($°C·10^{11} m^{-3}$)	d ($°C·s·m^{-1}$)
El Niño	−0.13	0.32	$−1.1 \times 10^{-15}$	3.8
La Niña	−0.01	−0.03	3.49×10^{-15}	−0.47

Also, we implement this model utilizing one, two, three and four factors to assess the sensitivity of our prediction to each factor. This approach enables us to evaluate the model's actual skill in predicting both the amplitude and structure of ENSO events. The prediction skill of the statistical model forecast is quantified using the anomaly correlation coefficient (ACC, Equation (2)) and explained variance (R^2, Equation (3)). These metrics are chosen as they provide complementary insights into the performance of the model. ACC captures the correlation between predicted and observed anomalies, and R^2 measures the proportion of variance in the observed data explained by the model prediction.

$$ACC = \frac{\sum_{t=1}^{T} \hat{y}_t y_t}{\sqrt{\sum_{t=1}^{T} \hat{y}_t^2} \sqrt{\sum_{t=1}^{T} y_t^2}}, \tag{2}$$

$$R^2 = 1 - \frac{\sum_{t=1}^{T} \left(\hat{y}_t - \bar{\hat{y}}\right)^2}{\sum_{t=1}^{T} \left(y - \bar{y}\right)^2}, \tag{3}$$

where $\hat{y}_t$ and y_t indicate the predicted and observed values at time *t*, respectively, and the overbar denotes the temporal mean. The leave-one-out cross-validation scheme is employed to mitigate overfitting concerns [75]. This approach systematically assesses the model's performance by iteratively training the model on all data points except one and then evaluating it on the omitted data point. This process is repeated for each data point in the dataset, and a comprehensive assessment of the model's generalization ability can be obtained without depending solely on a single split of the data.

Figure 8 provides a summary of the statistical model's performance in predicting the tropical Pacific SSTA in winter. When the four spring factors are used, high ACC and R^2 values dominate in the tropical central-to-eastern Pacific (Figure 8a,f), suggesting that the model shows high prediction skill in both ENSO phase and amplitude. When including the four factors, the model's prediction skill is higher than that obtained by using any single factor. For instance, using PR_{MAM}^{MC} as a single predictor yields high ACC and R^2 values in the off-equatorial northeastern Pacific and southeastern Pacific (Figure 8b,g), and PR_{MAM}^{WNP} leads to high ACC and R^2 values over the equatorial central-to-eastern Pacific (Figure 8c,h). These areas of maximum ACC and R^2 align with our earlier analysis regarding how tropical Pacific SSTA evolves with each spring precipitation pattern. Either WWV or UO makes the model's prediction skill limited to a narrow belt between the dateline and 120° W along the equator (Figure 8d,e,i,j), wherein the prediction skill from WWV is higher.
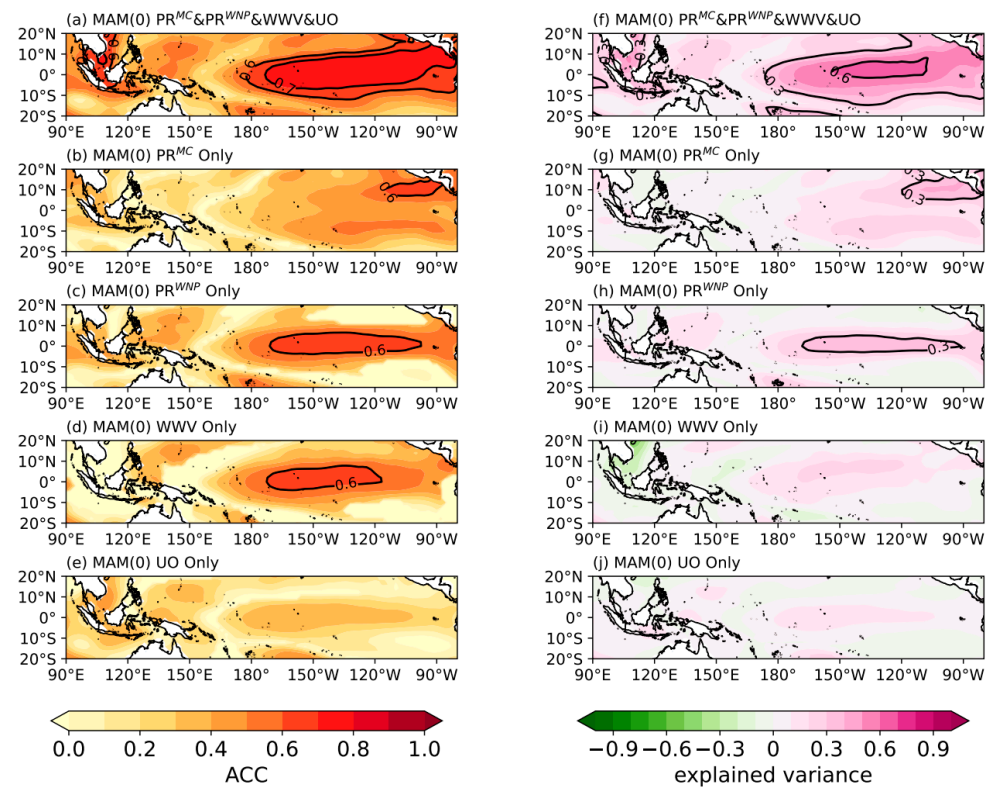
Figure 8. Distributions of anomaly correlation coefficient (ACC, **left** panel) between the observed and predicted winter (D^0JF^1) sea surface temperature anomalies (SSTA) in the tropical Pacific using the spring (MAM^0) factors as indicated. **Right** panel is similar to the left, but for the explained variance (R^2).

Due to the limited sample size in the observed ENSO events, the leave-one-out cross-validation scheme is further applied to reduce the overfitting of our model, similar to previous studies [70,76]. The model undergoes cross-validation by training across all El Niño/La Niña years, excluding one year under examination. Figure 9 displays the explained variance and root-mean-square error (RMSE) of the predicted winter Niño-3.4 indices when any single El Niño or La Niña year is excluded from the training dataset. It illustrates that the explained variance of the El Niño forecast consistently exceeds 55%, and meanwhile, RMSE remains below 0.4 °C (Figure 9a). Notably, the La Niña-trained model exhibits higher performance compared to the El Niño-trained model (Figure 9b). When excluding any one La Niña year from the training data, the explained variance consistently exceeds 65%, and the RMSE remains below 0.2 °C, indicating remarkable stability in prediction. The coefficients (*a*, *b*, *c*, *d*) for the 1-year cross-validation of El Niño and La Niña prediction are detailed in Tables 4 and 5, respectively. These coefficients demonstrate minimal sensitivity to specific training samples and closely resemble those obtained from the full hindcast model. For instance, the coefficient *b* for El Niño ranges from 0.22 to 0.42 in the 1-year cross-validation, mirroring the value of 0.32 in the hindcast model (Table 3). Thus, the established statistical model exhibits robustness during the current period, as demonstrated by 1-year cross-validation, despite the limited samples available for ENSO events.
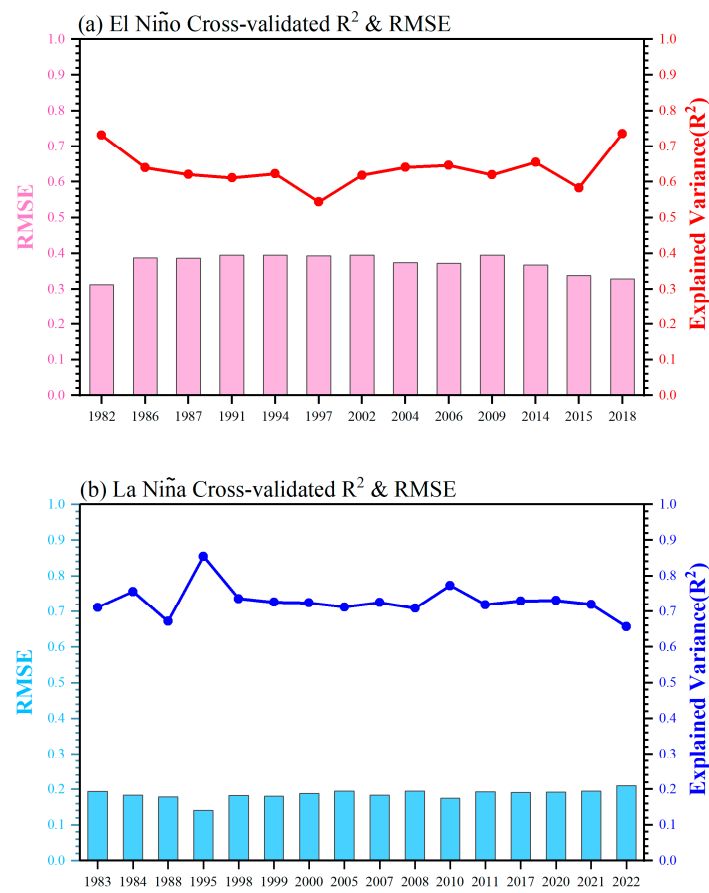
Figure 9. The values of R^2 (lines) and RMSE (bars) for every indicated (**a**) El Niño and (**b**) La Niña year cross validated.

Table 4. The optimized coefficients (*a*, *b*, *c*, *d*) of 1982–2022 El Niño events for 1-year cross validation and the predicted Niño-3.4 values in the El Niño prediction model.

El Niño Years	a (°C·mm^{-1})	b (°C·mm^{-1})	c (°C·10^{11}m^{-3})	d (°C·s·m^{-1})	Niño-3.4 (°C)
1982/83	-0.28	0.35	-3.33×10^{-15}	4.63	1.02
1986/87	-0.23	0.33	-2.22×10^{-15}	4.44	-0.35
1987/88	-0.05	0.36	-0.73×10^{-15}	4.03	0.38
1991/92	-0.13	0.30	-0.99×10^{-15}	3.8	1.30
1994/95	-0.13	0.30	-0.72×10^{-15}	3.72	0.08
1997/98	-0.16	0.31	-0.79×10^{-15}	4.01	2.34
2002/03	-0.13	0.32	-1.17×10^{-15}	3.87	0.82
2004/05	-0.14	0.34	-1.78×10^{-15}	3.89	1.02
2006/07	-0.09	0.29	-1.31×10^{-15}	4.26	1.25
2009/10	-0.13	0.32	-0.97×10^{-15}	3.62	1.48
2014/15	-0.14	0.23	0.99×10^{-15}	2.86	1.27
2015/16	0.01	0.22	0.66×10^{-15}	2.68	1.49
2018/19	-0.09	0.42	-1.22×10^{-15}	3.61	1.54

Table 5. Same as Table 4, but for La Niña events.

La Niña Years	a ($°C\ mm^{-1}$)	b ($°C\ mm^{-1}$)	c ($°C·10^{11}m^{-3}$)	d ($°C·s·m^{-1}$)	Niño-3.4 ($°C$)
1983/84	−0.09	−0.07	3.49×10^{-15}	−0.25	−0.13
1984/85	−0.15	−0.01	3.33×10^{-15}	−0.09	−1.18
1988/89	−0.12	−0.04	2.79×10^{-15}	0.03	−1.09
1995/96	−0.08	−0.14	3.79×10^{-15}	−0.12	−1.07
1998/99	−0.01	−0.04	3.83×10^{-15}	−0.35	−1.42
1999/00	−0.01	−0.06	3.19×10^{-15}	−0.28	−1.06
2000/01	−0.04	−0.04	3.32×10^{-15}	−0.40	−0.56
2005/06	−0.06	−0.05	3.4×10^{-15}	−0.27	−0.51
2007/08	−0.08	−0.04	3.13×10^{-15}	−0.16	−0.98
2008/09	−0.07	−0.05	3.35×10^{-15}	−0.22	−0.34
2010/11	0.01	−0.05	3.57×10^{-15}	−0.63	−0.83
2011/12	−0.06	−0.05	3.41×10^{-15}	−0.23	−0.44
2017/18	−0.10	−0.05	3.22×10^{-15}	−0.09	−0.09
2020/21	−0.08	−0.06	3.32×10^{-15}	−0.15	−0.83
2021/22	−0.08	−0.05	3.32×10^{-15}	−0.14	−0.29
2022/23	−0.07	−0.01	3.04×10^{-15}	−0.15	−0.65

3.6. Practical Utility of the Established Model

Based on the effective atmospheric and oceanic precursors, we have established a robust statistical model for predicting ENSO phase and amplitude. To assess its practical performance, we apply the model for ENSO prediction based on phases predicted by the NCEP Coupled Forecast System version 2 (CFSv2), as in Xuan et al. [71]. Specifically, we calculate the Niño-3.4 (D^0JF^1) index for all years predicted as El Niño, neutral or La Niña with a 7-month lead in our statistical forecast model. To objectively quantify its utility, we evaluate the model's performance across all predicted years using metrics such as R^2, correlation coefficient (*r*) and RMSE, as depicted in Figure 10. The correlation coefficient *r* increases from 0.74 in the CFSv2 to 0.86 in our model, and the explained variance increases from 43% to 75%, while RMSE decreases from 0.82 °C to 0.53 °C (Figure 10b). Overall, our model outperforms CFSv2 predictions by providing more accurate predictions of ENSO phase and amplitude while also demonstrating greater robustness. For example, the neutral winters of 2001 and 2012 were predicted as El Niño in the CFSv2 (red dots with gray circle and cross in Figure 10a), while they are neutral states in our model (gray dots in Figure 10b). Honestly, it has the potential to mitigate errors to some extent for years anticipated to be in neutral states but predicted as ENSO events. However, our model does not perform as well for years expected to exhibit warm or cold ENSO phases but end up in neutral states, such as in 1993. The unpredictability of these events may be attributed to strong extra-tropical noise disturbances during the middle and end of the year [77,78].

Since our model prediction relies on the phase prediction of the NCEP CFSv2 model, the performance of CFSv2 can determine our prediction skill to a large extent. Encouragingly, the NCEP CFSv2 dynamical model has achieved successful predictions for the majority of ENSO years, correctly forecasting 10 out of 13 El Niño events and 11 out of 16 La Niña events with a 7-month leading time during the period from 1982 to 2022. With ongoing advancements in ENSO phase prediction, our model for ENSO amplitude prediction is expected to provide even more valuable information in the future.
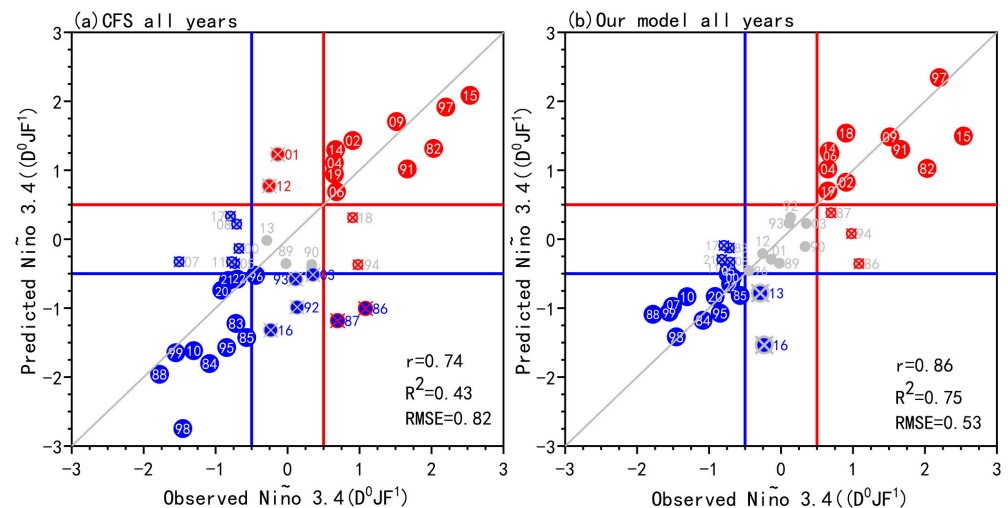
Figure 10. (**a**) Scatterplot between the observed and predicted Niño-3.4 index (D^0JF^1) from NCEP CFSv2 for El Niño (red dots), La Niña (blue dots) and neutral (gray dots) years with a 7-month leading time. (**b**) Scatterplot between the observed and predicted Niño-3.4 index (D^0JF^1) by our statistical model. Dots with circles and crosses represent the correctly and falsely predicted El Niño (red) and La Niña (blue), respectively. In the cases of the circles with crosses, the circle color denotes the observed phase.

4. Summary and Discussion

This study investigated the characteristics of spring precipitation over the Maritime Continent (MC) and Western North Pacific (WNP) and their influence on the evolution of ENSO. Spring precipitation anomalies over the MC and WNP exhibit two distinct modes: a zonal dipole mode between the equatorial MC and western Pacific and a tilted meridional dipole mode across the WNP and central Pacific south of the equator (Figure 2). These modes correspond to different ENSO evolution patterns, with the zonal mode typically occurring during the second spring of a multi-year La Niña event or rapid decaying spring of El Niño events, while the tilted meridional mode tends to occur in the spring of El Niño onset year.

The composite analysis based on the spring precipitation patterns shows three different ENSO evolution patterns, which offers valuable insights into the post-spring development of ENSO. The anomalous precipitation influences the zonal wind field, which in turn affects zonal sea currents, ultimately changing SST in the equatorial central-to-eastern Pacific. The slow decaying of La Niña in the subsequent spring is associated with more MC precipitation and less precipitation over the equatorial central-to-western Pacific that can persist in the following seasons (Figure 4). As a result, anomalous easterlies occur over the equatorial central Pacific, further exciting upwelling oceanic Kelvin waves to the shallow thermocline and maintaining the cooling tendency.

A rapid decay of El Niño occurs when spring MC precipitation is less, and the central Pacific south of the equator experiences more rainfall. Such a southward shift of precipitation induces westerly anomalies shifting south of the equator, which can further enhance northward Sverdrup transports [68] and accelerate the discharge process of oceanic heat content. Meanwhile, the enhanced poleward Sverdrup transports decrease the sea level height in the central Pacific, and the anomalous westward pressure gradient force consequently intensifies to reverse the surface current anomalies to flow westwards from the cold tongue. Therefore, El Niño experiences a rapid decay and transitions to La Niña. The main difference between the decays of La Niña and El Niño arises from the absence or presence of the southward shift of zonal wind anomalies. During La Niña mature winter and decaying spring, there is no evident southward shift in the weak easterly anomalies (Figure 4l,m). The equatorward Sverdrup transports are thus weak and have no evident acceleration in the decaying spring, which leads to a slow decay rather than a phase transition.

Increased precipitation over the WNP in spring is associated with the development of positive NPMM (Figure 6j), and anomalous westerlies are generated over the equatorial western Pacific. Meanwhile, the equatorial Pacific is recharged and occupied by anomalous eastward currents driven by the westerly anomalies (Figure 6r). In such a situation, oceanic conditions favor the onset of El Niño. Similarly, the La Niña event analyzed above develops from a negative NPMM (Figure 4i), the associated equatorial WWV is anomalously negative and sea current anomalies are westwards (Figure 4q), mirroring those during the onset of El Niño.

Combining these spring precipitation signals and the anomalous WWV and zonal sea current, a simple statistical model is established, aiming at predicting ENSO states in the subsequent winter. Although relying on the prediction of the ENSO phase in the NCEP CFSv2, our simple model performs better than CFSv2 in predicting the ENSO phase and amplitude in a 7-month leading time. Utilizing ENSO predictions in our statistical model, the prediction can explain approximately 75% of the total variance of Niño-3.4 SSTA during the ENSO peak phase, with a correlation coefficient (r) of 0.86 and RMSE of 0.54 °C (Figure 10b). Despite the limited sample size of ENSO events, our model exhibits robustness through leave-one-year-out cross-validation.

However, the practical utility of this simple model is constrained by the phase prediction of the NCEP CFSv2 model, as discussed in Section 3.6. Prediction inaccuracies may arise from prediction errors, including model errors and initial condition errors [79,80]. This simple ENSO prediction model is expected to play a promising role as dynamical models.

References

1. McPhaden, M.J.; Zebiak, S.E.; Glantz, M.H. ENSO as an integrating concept in earth science. *Science* **2006**, *314*, 1740–1745. [CrossRef] [PubMed]
2. Philander, S.G.H.; Yamagata, T.; Pacanowski, R.C. Unstable Air-Sea Interactions in the Tropics. *J. Atmos. Sci.* **1984**, *41*, 604–613. [CrossRef]
3. Ropelewski, C.F.; Halpert, M.S. Global and regional scale precipitation patterns associated with the El Niño/Southern Oscillation. *Mon. Weather Rev.* **1987**, *115*, 1606–1626. [CrossRef]
4. Ramage, C.S. Role of a tropical "maritime continent" in the atmospheric circulation. *Mon. Weather Rev.* **1968**, *96*, 365–370. [CrossRef]

5. Philander, S.G.H. El Nino southern oscillation phenomena. *Nature* **1983**, *302*, 295–301. [CrossRef]

6. Hamada, J.I.; Yamanaka, D.M.; Matsumoto, J.; Fukao, S.; Winarso, P.A.; Sribimawati, T. Spatial and temporal variations of the rainy season over Indonesia and their link to ENSO. *J. Meteorol. Soc. Jpn. Ser. II* **2002**, *80*, 285–310. [CrossRef]

7. Chang, C.P.; Wang, Z.; Ju, J.H.; Li, T. On the relationship between western maritime continent monsoon rainfall and ENSO during northern winter. *J. Clim.* **2004**, *17*, 665–672. [CrossRef]

8. Liu, J.; Da, Y.; Li, T.; Hu, F. Impact of ENSO on MJO Pattern Evolution over the Maritime Continent. *J. Meteorol. Res.* **2020**, *34*, 1151–1166. [CrossRef]

9. Wang, B.; Wu, R.; Fu, X. Pacific–East Asian teleconnection: How does ENSO affect East Asian climate? *J. Clim.* **2000**, *13*, 1517–1536. [CrossRef]

10. Wu, R.; Hu, Z.Z.; Kirtman, B.P. Evolution of ENSO-related rainfall anomalies in East Asia. *J. Clim.* **2003**, *16*, 3742–3758. [CrossRef]

11. Dayem, K.E.; Noone, D.C.; Molnar, P. Tropical western Pacific warm pool and maritime continent precipitation rates and their contrasting relationships with the Walker Circulation. *J. Geophys. Res. Atmos.* **2007**, *112*, D06101. [CrossRef]

12. McCreary, J.P.; Anderson, D.L.T. A simple model of El Nino and the Southern Oscillation. *Mon. Weather Rev.* **1984**, *112*, 934–946. [CrossRef]

13. Suarez, M.J.; Schopf, P.S. A delayed action oscillator for ENSO. *J. Atmos. Sci.* **1988**, *45*, 3283–3287. [CrossRef]

14. Battisti, D.S. Dynamics and thermodynamics of a warming event in a coupled tropical atmosphere–ocean model. *J. Atmos. Sci.* **1988**, *45*, 2889–2919. [CrossRef]

15. Chiang, J.C.H.; Vimont, D.J. Analogous Pacific and Atlantic meridional modes of tropical atmosphere–ocean variability. *J. Clim.* **2004**, *17*, 4143–4158. [CrossRef]

16. Xie, R.H.; Huang, F.; Ren, H. Subtropical air-sea interaction and development of central Pacific El Niño. *J. Ocean Univ. China* **2013**, *12*, 260–271. [CrossRef]

17. Ding, R.Q.; Li, J.P.; Tseng, Y.H.; Cheng, S.; Guo, Y.P. The Victoria mode in the North Pacific linking extratropical sea level pressure variations to ENSO. *J. Geophys. Res. Atmos.* **2015**, *120*, 27–45. [CrossRef]

18. Ding, R.Q.; Li, J.P.; Tseng, Y.H.; Xie, F. Joint impact of North and South Pacific extratropical atmospheric variability on the onset of ENSO events. *J. Geophys. Res. Atmos.* **2017**, *122*, 279–298. [CrossRef]

19. Wu, B.; Li, T.; Zhou, T. Asymmetry of atmospheric circulation anomalies over the western North Pacific between El Niño and La Niña. *J. Clim.* **2010**, *23*, 4807–4822. [CrossRef]

20. Stuecker, M.F.; Timmermann, A.; Jin, F.F.; McGregor, S.; Ren, H.L. A combination mode of the annual cycle and the El Niño/Southern Oscillation. *Nat. Geosci.* **2013**, *6*, 540–544. [CrossRef]

21. Stuecker, M.F.; Jin, F.F.; Timmermann, A.; McGregor, S. Combination mode dynamics of the anomalous northwest Pacific anticyclone. *J. Clim.* **2015**, *28*, 1093–1111. [CrossRef]

22. Zhang, W.; Li, H.; Jin, F.F.; Stuecker, M.F.; Turner, A.G.; Klingaman, N.P. The annual-cycle modulation of meridional asymmetry in ENSO's atmospheric response and its dependence on ENSO zonal structure. *J. Clim.* **2015**, *28*, 5795–5812. [CrossRef]

23. Furtado, J.C.; Anderson, B.T.; Schneider, N. Linkages between the North Pacific Oscillation and central tropical Pacific SSTs at low frequencies. *Clim. Dyn.* **2012**, *39*, 2833–2846. [CrossRef]

24. Park, J.Y.; Yeh, S.W.; Kug, J.S.; Yoon, J. Favorable connections between seasonal footprinting mechanism and El Niño. *Clim. Dyn.* **2013**, *40*, 1169–1181. [CrossRef]

25. You, Y.; Furtado, J.C. The South Pacific Meridional Mode and Its Role in Tropical Pacific Climate Variability. *J. Clim.* **2018**, *31*, 10141–10163. [CrossRef]

26. Amaya, D.J. The Pacific meridional mode and ENSO: A review. *Curr. Clim. Change Rep.* **2019**, *5*, 296–307. [CrossRef]

27. Gill, A.E. Some simple solutions for heat-induced tropical circulation. *Q. J. R. Meteorol. Soc.* **1980**, *106*, 447–462.

28. Zhao, J.; Kug, J.S.; Park, J.H.; An, S.I. Diversity of North Pacific Meridional Mode and its distinct impacts on El Niño-Southern Oscillation. *Geophys. Res. Lett.* **2020**, *47*, e2020GL088993. [CrossRef]

29. Zhang, Y.; Yu, S.Y.; Amaya, D.J.; Kosaka, Y.; Larson, S.M.; Wang, X.D.; Jun, C.Y. Pacific meridional modes without equatorial pacific influence. *J. Clim.* **2021**, *34*, 5285–5301. [CrossRef]

30. Wang, C.; Weisberg, R.H.; Virmani, J.I. Western Pacific interannual variability associated with the El Niño-Southern Oscillation. *J. Geophys. Res.* **1999**, *104*, 5131–5149. [CrossRef]

31. Wang, C. A review of ENSO theories. *Nat. Sci. Rev.* **2018**, *5*, 813–825. [CrossRef]

32. McGregor, S.; Timmermann, A.; Schneider, N.; Stuecker, M.F.; England, M.H. The effect of the South Pacific Convergence Zone on the termination of El Nino events and the meridional asymmetry of ENSO. *J. Clim.* **2012**, *25*, 5566–5586. [CrossRef]

33. McGregor, S.; Ramesh, N.; Spence, P.; England, M.H.; McPhaden, M.J.; Santoso, A. Meridional movement of wind anomalies during ENSO events and their role in event termination. *Geophys. Res. Lett.* **2013**, *40*, 749–754. [CrossRef]

34. McGregor, S.; Spence, P.; Schwarzkopf, F.U.; England, M.H.; Santoso, A.; Kessler, W.S.; Timmermann, A.; Böning, C.W. ENSO-driven interhemispheric Pacific mass transports. *J. Geophys. Res. Ocean* **2014**, *119*, 6221–6237. [CrossRef]

35. Abellán, E.; McGregor, S. The role of the southward wind shift in both the seasonal synchronization and duration of ENSO events. *Clim. Dyn.* **2016**, *47*, 509–527. [CrossRef]

36. Xie, R.H.; Mu, M.; Fang, X. New indices for better understanding ENSO by incorporating convection sensitivity to sea surface temperature. *J. Clim.* **2020**, *33*, 7045–7061. [CrossRef]

37. Gong, Y.; Li, T. Mechanism for Southward Shift of Zonal Wind Anomalies during the Mature Phase of ENSO. *J. Clim.* **2021**, *34*, 8897–8911. [CrossRef]

38. Jin, F.F. An equatorial ocean recharge paradigm for ENSO. Part I: Conceptual model. *J. Atmos. Sci.* **1997**, *54*, 811–829. [CrossRef]

39. Jin, F.F. An equatorial ocean recharge paradigm for ENSO. Part II: A stripped-down coupled model. *J. Atmos. Sci.* **1997**, *54*, 830–847. [CrossRef]

40. Meinen, C.S.; McPhaden, M.J. Observations of warm water volume changes in the equatorial Pacific and their relationship to El Niño and La Niña. *J. Clim.* **2000**, *13*, 3551–3559. [CrossRef]

41. Tseng, Y.H.; Hu, Z.Z.; Ding, R.Q.; Chen, H.C. An ENSO prediction approach based on ocean conditions and ocean–atmosphere coupling. *Clim. Dyn.* **2017**, *48*, 2025–2044. [CrossRef]

42. Kug, J.S.; Jin, F.F.; And, S.I. Two Types of El Niño Events: Cold Tongue El Niño and Warm Pool El Niño. *J. Clim.* **2009**, *22*, 1499–1515. [CrossRef]

43. Chen, H.C.; Hu, Z.Z.; Huang, B.H.; Sui, C.H. The role of reversed equatorial zonal transport in terminating an ENSO event. *J. Clim.* **2016**, *29*, 5859–5877. [CrossRef]

44. Ren, H.L.; Lu, B.; Wan, J.H.; Tian, B.; Zhang, P.Q. Identification standard for ENSO events and its application to climate monitoring and prediction in China. *J. Meteorol. Res.* **2018**, *32*, 923–936. [CrossRef]

45. Guan, C.; McPhaden, M.J.; Wang, F.; Hu, S. Quantifying the role of oceanic feedbacks on ENSO asymmetry. *Geophys. Res. Lett.* **2019**, *46*, 2140–2148. [CrossRef]

46. Zhang, C.; Luo, J.J.; Li, S. Impacts of tropical Indian and Atlantic Ocean warming on the occurrence of the 2017/2018 La Niña. *Geophys. Res. Lett.* **2019**, *46*, 3435–3445. [CrossRef]

47. Ren, H.L.; Jin, F.F. Recharge oscillator mechanisms in two types of ENSO. *J. Clim.* **2013**, *26*, 6506–6523. [CrossRef]

48. Jin, F.-F.; An, S.I. Thermocline and zonal advective feedbacks within the equatorial ocean recharge oscillator model for ENSO. *Geophys. Res. Lett.* **1999**, *26*, 2989–2992. [CrossRef]

49. Adler, R.F.; Huffman, G.J.; Chang, A.; Ferraro, R.; Xie, P.P.; Janowiak, J.; Rudolf, B.; Schneider, U.; Curtis, S.; Bolvin, D.; et al. The Version-2 Global Precipitation Climatology Project (GPCP) Monthly Precipitation Analysis (1979–Present). *J. Hydrometeor.* **2003**, *4*, 1147–1167. [CrossRef]

50. Kanamitsu, M.; Ebisuzaki, W.; Woollen, J.S.; Yang, S.; Hnilo, J.J.; Fiorino, M.; Potter, G. NCEP–DOE AMIP-II Reanalysis (R-2). *Bull. Am. Meteorol. Soc.* **2002**, *83*, 1631–1643. [CrossRef]

51. Huang, B.; Thorne, P.W.; Banzon, V.F.; Boyer, T.; Chepurin, G.; Lawrimore, J.H.; Menne, M.J.; Smith, T.M.; Vose, R.S.; Zhang, H. Extended Reconstructed Sea Surface Temperature, Version 5 (ERSSTv5): Upgrades, Validations, and Intercomparisons. *J. Clim.* **2017**, *30*, 8179–8205. [CrossRef]

52. Behringer, D.; Xue, Y. Evaluation of the Global Ocean Data Assimilation system at NCEP: The Pacific Ocean. In Proceedings of the Eighth Symposium on Integrated Observing and Assimilation System for Atmosphere, Oceans, and Land Surface, AMS 84th Annual Meeting, Washington State Convection and Trade Center, Seattle, DC, USA, 11–15 January 2004.

53. Rasmusson, E.M.; Carpenter, T.H. Variations in tropical sea surface temperature and surface wind fields associated with the Southern Oscillation/El Niño. *Mon. Wea. Rev.* **1982**, *110*, 354–384. [CrossRef]

54. Bretherton, C.S.; Smith, C.; Wallace, J.M. An intercomparison of methods for finding coupled patterns in climate data. *J. Clim.* **1992**, *5*, 541–560. [CrossRef]

55. Wallace, J.M.; Smith, C.; Bretherton, C.S. Singular value decomposition of wintertime sea surface temperature and 500-mb height anomalies. *J. Clim.* **1992**, *5*, 561–576. [CrossRef]

56. Varotsos, C.A.; Tzanis, C.G.; Sarlis, N.V. On the progress of the 2015–2016 El Niño event, Atmos. *Chem. Phys.* **2016**, *16*, 2007–2011.

57. Chen, L.; Li, T.; Wang, B.; Wang, L. Formation mechanism for 2015/16 super El Niño. *Sci. Rep.* **2017**, *7*, 2975. [CrossRef] [PubMed]

58. L'Heureux, M.L.; Takahashi, K.; Watkins, A.B.; Barnston, A.G.; Becker, E.J.; Di Liberto, T.E.; Gamble, F.; Gottschalck, J.; Halpert, M.S.; Huang, B.; et al. Observing and Predicting the 2015/16 El Niño. *Bull. Am. Meteorol. Soc.* **2017**, *98*, 1363–1382. [CrossRef]

59. Santoso, A.; Mcphaden, M.J.; Cai, W. The defining characteristics of ENSO extremes and the strong 2015/2016 El Niño. *Rev. Geophys.* **2017**, *55*, 1079–1129. [CrossRef]

60. Zhai, P.; Yu, R.; Guo, Y.; Li, Q.; Ren, X.; Wang, Y.; Xu, W.; Liu, Y.; Ding, Y. The strong El Niño of 2015/16 and its dominant impacts on global and China's climate. *J. Meteorol. Res.* **2016**, *30*, 283–297. [CrossRef]

61. Capotondi, A.; Wittenberg, A.T.; Newman, M.; Di Lorenzo, E.; Yu, J.; Braconnot, P.; Cole, J.; Dewitte, B.; Giese, B.; Guilyardi, E.; et al. Understanding ENSO diversity. *Bull. Am. Meteorol. Soc.* **2015**, *96*, 921–938. [CrossRef]

62. Okumura, Y.M. ENSO Diversity from an Atmospheric Perspective. *Curr. Clim. Change Rep.* **2019**, *5*, 245–257. [CrossRef]

63. Kessler, W.S.; McPhaden, M.J. Oceanic equatorial waves and the 1991–93 El Niño. *J. Clim.* **1995**, *8*, 1757–1774. [CrossRef]

64. Hu, S.; Fedorov, A.V. Indian Ocean warming can strengthen the Atlantic meridional overturning circulation. *Nat. Clim. Change* **2019**, *9*, 747–751. [CrossRef]

65. Pegion, K.; Alexander, M. The seasonal footprinting mechanism in CFSv2: Simulation and impact on ENSO prediction. *Clim. Dyn.* **2013**, *41*, 1671–1683. [CrossRef]

66. Pegion, K.V.; Selman, C.M. Extratropical precursors of the El Niño–Southern Oscillation. In *Climate Extremes: Patterns and Mechanisms*, 1st ed.; Wang, S., Yoon, J., Funk, C., Gillies, R., Eds.; John Wiley and Sons: Hoboken, NJ, USA, 2017; pp. 299–314.

67. Gong, Y.; Li, T. Comparison of southward shift mechanisms of equatorial westerly anomalies between EP and CP El Niño. *Clim. Dyn.* **2023**, *60*, 785–796. [CrossRef]

68. Kug, J.-S.; Kang, I.S.; An, S.I. Symmetric and antisymmetric mass exchanges between the equatorial and off-equatorial Pacific associated with ENSO. *J. Geophys. Res.* **2003**, *108*, 3284. [CrossRef]

69. Hu, Z.; Kumar, A.; Huang, B.; Zhu, J.; Zhang, R.; Jin, F. Asymmetric evolution of El Niño and La Niña: The recharge/discharge processes and role of the off-equatorial sea surface height anomaly. *Clim. Dyn.* **2017**, *49*, 2737–2748. [CrossRef]

70. Lai, A.W.C.; Herzog, M.; Graf, H.F. ENSO forecasts near the spring predictability barrier and possible reasons for the recently reduced predictability. *J. Clim.* **2018**, *31*, 815–838.

71. Xuan, Z.L.; Zhang, W.J.; Jiang, F.; Jin, F.F. Effective ENSO amplitude forecasts based on oceanic and atmospheric preconditions. *J. Clim.* **2022**, *35*, 3279–3291. [CrossRef]

72. Varotsos, C.; Sarlis, N.V.; Mazei, Y.; Saldaev, D.; Efstathiou, M. A Composite Tool for Forecasting El Niño: The Case of the 2023–2024 Event. *Forecasting* **2024**, *6*, 187–203. [CrossRef]

73. Karamperidou, C.; Cane, M.A.; Lall, U.; Wittenberg, A.T. Intrinsic modulation of ENSO predictability viewed through a local Lyapunov lens. *Clim. Dyn.* **2014**, *42*, 253–270. [CrossRef]

74. Hou, Z.; Li, J.; Ding, R.; Karamperidou, C.; Duan, W.; Liu, T.; Feng, J. Asymmetry of the predictability limit of the warm ENSO phase. *Geophys. Res. Lett.* **2018**, *45*, 7646–7653. [CrossRef]

75. Elsner, J.B.; Schmertmann, C.P. Assessing forecast skill through cross validation. *Wea. Forecast.* **1994**, *9*, 619–624. [CrossRef]

76. Seleznev, A.; Mukhin, D. Improving statistical prediction and revealing nonlinearity of ENSO using observations of ocean heat content in the tropical Pacific. *Clim. Dyn.* **2023**, *60*, 1–15. [CrossRef]

77. Su, J.Z.; Xiang, B.; Wang, B.; Li, T. Abrupt termination of the 2012 Pacific warming and its implication on ENSO prediction. *Geophys. Res. Lett.* **2014**, *41*, 9058–9064. [CrossRef]

78. Yu, S.; Fedorov, A. The role of westerly wind bursts during different seasons versus ocean heat recharge in the development of extreme El Niño in climate models. *Geophys. Res. Lett.* **2020**, *47*, e2020GL088381. [CrossRef]

79. Tao, L.J.; Zhang, R.H.; Gao, C. Initial error-induced optimal perturbations in ENSO predictions, as derived from an intermediate coupled model. *Adv. Atmos. Sci.* **2017**, *34*, 791–803. [CrossRef]

80. Larson, S.M.; Kirtman, B.P. Drivers of coupled model ENSO error dynamics and the spring predictability barrier. *Clim. Dyn.* **2017**, *48*, 3631–3644. [CrossRef]